



# High-resolution (375 m) cloud microstructure as seen from the NPP/VIIRS satellite imager

D. Rosenfeld<sup>1</sup>, G. Liu<sup>2</sup>, X. Yu<sup>2</sup>, Y. Zhu<sup>2</sup>, J. Dai<sup>2</sup>, X. Xu<sup>2</sup>, and Z. Yue<sup>3</sup>

<sup>1</sup>Institute of Earth Sciences, The Hebrew University of Jerusalem, Israel

<sup>2</sup>Meteorological Institute of Shaanxi Province, Xi'an 710015, China

<sup>3</sup>Center of Weather Modification of Shaanxi Province, Xi'an 710015, China

Correspondence to: D. Rosenfeld (daniel.rosenfeld@mail.huji.ac.il)

Received: 13 September 2013 – Published in Atmos. Chem. Phys. Discuss.: 13 November 2013

Revised: 20 January 2014 – Accepted: 30 January 2014 – Published: 10 March 2014

**Abstract.** VIIRS (Visible Infrared Imaging Radiometer Suite), onboard the Suomi NPP (National Polar-orbiting Partnership) satellite, has an improved resolution of 750 m with respect to the 1000 m of the Moderate Resolution Imaging Spectroradiometer for the channels that allow retrieving cloud microphysical parameters such as cloud drop effective radius ( $r_e$ ). VIIRS also has an imager with five channels of double resolution of 375 m, which was not designed for retrieving cloud products. A methodology for a high-resolution retrieval of  $r_e$  and microphysical presentation of the cloud field based on the VIIRS imager was developed and evaluated with respect to MODIS in this study. The tripled microphysical resolution with respect to MODIS allows obtaining new insights for cloud–aerosol interactions, especially at the smallest cloud scales, because the VIIRS imager can resolve the small convective elements that are sub-pixel for MODIS cloud products. Examples are given for new insights into ship tracks in marine stratocumulus, pollution tracks from point and diffused sources in stratocumulus and cumulus clouds over land, deep tropical convection in pristine air mass over ocean and land, tropical clouds that develop in smoke from forest fires and in heavy pollution haze over densely populated regions in southeastern Asia, and for pyrocumulonimbus clouds.

It is found that the VIIRS imager provides more robust physical interpretation and refined information for cloud and aerosol microphysics as compared to MODIS, especially in the initial stage of cloud formation. VIIRS is found to identify significantly more fully cloudy pixels when small boundary layer convective elements are present. This, in turn, al-

lows for a better quantification of cloud–aerosol interactions and impacts on precipitation-forming processes.

## 1 Introduction

The Suomi NPP (National Polar-orbiting Partnership) launched on 28 October 2011 inaugurated a new generation of operational US polar-orbiting satellites. Its primary imaging instrument is VIIRS (Visible Infrared Imaging Radiometer Suite). This study shows benefits of the added spatial resolution of the VIIRS imager with respect to the Moderate Resolution Imaging Spectroradiometer (MODIS). VIIRS has 22 visible–infrared channels that combine many of the best aspects of the NOAA Advanced Very High Resolution Radiometer (AVHRR), the Defense Meteorological Satellite Program (DMSP) Operational Linescan System (OLS), and the National Aeronautics and Space Administration (NASA) MODIS. VIIRS provides highly detailed imagery of global coverage, with multi-band imaging capabilities that support the acquisition of high-resolution atmospheric imagery for a variety of applications, including detection of cloud properties, fires, smoke, and atmospheric aerosols<sup>1</sup>. The sensor data records (SDRs) of VIIRS are composed of 5 bands of imagery resolution (375 m) and 17 bands of moderate resolution (750 m), and have been made publicly available since 2 July 2012 via the NOAA's Comprehensive Large Array-data Stewardship System (CLASS)<sup>2</sup>. In addition to the improved spatial resolution at nadir, the VIIRS footprint

<sup>1</sup><http://www.raytheon.com/capabilities/products/viirs/>

<sup>2</sup><http://www.class.ncdc.noaa.gov>

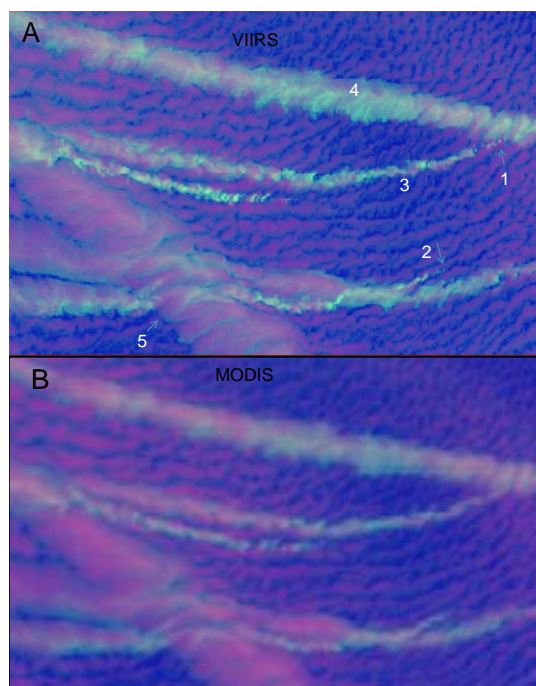


**Fig. 1.** Microphysical RGB composite imagery of ship tracks, as seen by VIIRS (22:20 UT, panel A) and MODIS (22:40 UT, panel B) overpasses on 15 July 2012 over the northeastern Pacific in an area of  $174 \text{ km} \times 107 \text{ km}$  centered at  $40.55^\circ \text{ N}$ ,  $140.09^\circ \text{ W}$ . The images show the same area and are scaled to show the full resolution of 375 m of the VIIRS imager. This results in a blurred picture of the ship track in the MODIS image due to its lower resolution of 1000 m.

at the cross-track dimension is kept nearly constant, even though the width of the swath is increased to overlap even at the Equator between consecutive orbits, thus providing full global coverage twice daily.

Many environmental data records (EDRs) have already been derived and further ones are being developed and tested now, including sea surface temperature, cloud properties, ocean color, aerosol characteristics, etc. The EDRs of these and other products have recently reached the “beta” stage of maturity and are on their way to further levels of quality control (Hillger et al., 2013).

Unlike the 1 km resolution of the infrared (IR) channels of MODIS and AVHRR, VIIRS has 375 m of spatial resolution in the IR imager bands, which represents a significant improvement over previous instruments. The benefit of the higher resolution becomes most evident when viewing the tops of small-scale features in the thermal channels. For example, smaller boundary layer clouds can be resolved by VIIRS as compared to MODIS or AVHRR, whose footprint area is 7 times larger than the NPP imager. Due to the improved resolution, smaller scale cloud tops can also be resolved with corresponding colder top temperatures as compared to lower resolution sensors. Hillger et al. (2013)

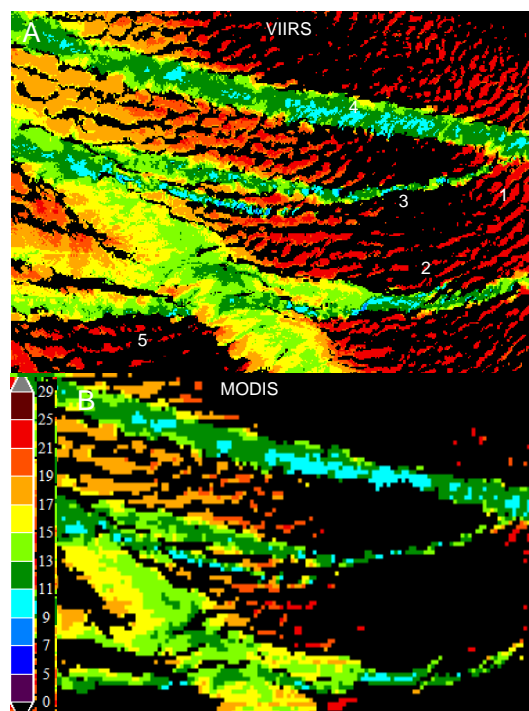


**Fig. 2.** VIIRS and MODIS retrieved  $r_e$  for the clouds shown in Fig. 1. Only clouds with  $0.6 \mu\text{m}$  solar reflectance  $> 0.3$  are analyzed.

showed that the coldest brightness temperature of a convective complex from GOES, MODIS, and VIIRS within a 2 min time difference was  $-79.7^\circ \text{ C}$ ,  $-86.9^\circ \text{ C}$ , and  $-90.6^\circ \text{ C}$ , respectively. They postulated the differences were due in part to the smaller pixel sizes of the instruments with better resolution, with VIIRS providing the most accurate estimate of the actual emitting temperature of the thunderstorm overshooting tops. Brunner et al. (2007) also tested the effect of different resolutions on the temperature observed by AVHRR, and suggested that the observed minimum temperature of an overshooting top would be 11 K warmer for the 8 km sampled distance than for the 1 km sampled distance.

Focusing attention on cloud products, during the last 20 yr, the technology of visible and IR satellite retrieval has been applied to retrieve cloud drop effective radius ( $r_e$ ), liquid water path (LWP), cloud optical depth (COD), cloud-top temperature ( $T$ ), and thermodynamic phase (ice, mixed phase, or water). In addition, cloud drop number concentration ( $N_c$ ) has been retrieved for marine layer clouds (e.g., Platnick et al., 2003).

Rosenfeld and Lensky (1998) used the retrieved  $T$  and  $r_e$  from AVHRR to investigate convective cloud microstructure and precipitation-forming processes using both qualitative and quantitative approaches. A microphysical red–green–blue (RGB) composite visualization was devised to qualitatively highlight the cloud composition. In the qualitative approach,  $T$  and  $r_e$  are visualized by modulating the blue and green components of the RGB composition, respectively.

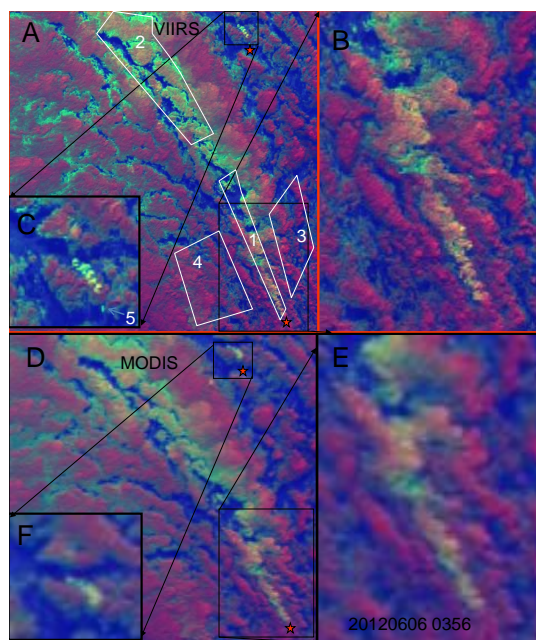


**Fig. 3.** Same as Fig. 1, but showing a pollution track from a coal power plant in Australia, as seen by VIIRS (03:56 UT, panel A) and MODIS (04:05 UT, panel D) overpasses on 6 June 2012, in an area of  $163 \text{ km} \times 154 \text{ km}$  centered at  $32.88^\circ \text{ S}$ ,  $149.20^\circ \text{ E}$ . The red stars show the origination points of a pollution track and a plume of smoky clouds from a small hot spot. These two features are magnified to VIIRS full resolution in panel (B) in an area of  $54 \text{ km} \times 58 \text{ km}$  centered at  $33.17^\circ \text{ S}$ ,  $149.90^\circ \text{ E}$  and (C) in an area of  $20 \text{ km} \times 18 \text{ km}$  centered at  $32.27^\circ \text{ S}$ ,  $149.43^\circ \text{ E}$ , respectively. The same magnification is applied to the MODIS image in panels (E) and (F).

The  $T$  is given by the  $10.8 \mu\text{m}$  brightness temperature, and the  $r_e$  is approximated by the  $3.7 \mu\text{m}$  solar reflectance component. The red is modulated by the visible reflectance. The qualitative approach was also applied to the geostationary satellite. With the rich spectral information of the SEVIRI instrument on the METEOSAT Second Generation (MSG) satellite, Lensky and Rosenfeld (2008) developed five RGB combinations to represent the additional information on microphysics of clouds in relation to the environmental and meteorological elements.

Furthermore, Rosenfeld and Lensky (1998) introduced a quantitative methodology for inferring precipitation-forming processes using vertical profiles of the effective radius of cloud particles, obtained by analyzing the  $T-r_e$  relations of convective clusters. Generally, the cloud drops nucleate near the convective cloud base, and gradually grow with height. Therefore, the cloudy pixels with the smallest  $r_e$  and highest  $T$  define the cloud base. Because the coalescence rate is proportional to  $r_e^5$ , the growth of  $r_e$  with decreasing  $T$  higher in the cloud above  $\sim 14 \mu\text{m}$  indicates initiation of rain (Freud and Rosenfeld, 2012). This methodology was also applied to other polar orbit satellite platforms. The underlying assump-



**Fig. 4.** An aerial view of two coal power plants at the location of the origin of the pollution track ( $33.38^\circ \text{ S}$ ,  $150.05^\circ \text{ E}$ ) that is shown in Fig. 3. The power plants are  $7 \text{ km}$  apart from each other.

tion of the method is that time and space are exchangeable, so the composition of the tops of various clouds reaching different heights in a convective cluster at a given time is similar to the time evolution of a cloud-top composition as it grows up with time. This assumption was validated by tracking the tops of growing clouds by rapid scans of a geostationary satellite (Lensky and Rosenfeld, 2006).

By virtue of the quantitative approaches from the satellite retrieval, a large number of applications can be gained by the retrieved microphysical properties, which are applied to

- detection of aircraft icing conditions (Schickel et al., 1994; Thompson et al., 1997);
- detection of fog or low clouds (d’Entremont and Thomason, 1987; Bendix et al., 2005);
- estimation of precipitation (Lensky and Rosenfeld, 1997; Rosenfeld and lensky, 1998);
- detection of severe convective storms (Rosenfeld et al., 2008; Lindsey et al., 2006), detection of the impacts of air heavy smoke (Rosenfeld et al., 2007), pollution (Rosenfeld et al., 2012a), dust (Rosenfeld et al., 2001), and salt (Rosenfeld et al., 2002; Rudich et al., 2002) on the precipitation-forming processes (Rosenfeld, 1999, 2000; Rosenfeld et al., 2012b);
- detection of glaciation temperature of clouds (Rosenfeld et al., 2011);
- investigation of the potential of cloud seeding for precipitation enhancement (Woodley et al., 2000; Rosenfeld and Woodley, 2003; Rosenfeld et al., 2005) and hail suppression (Rosenfeld et al., 2001).



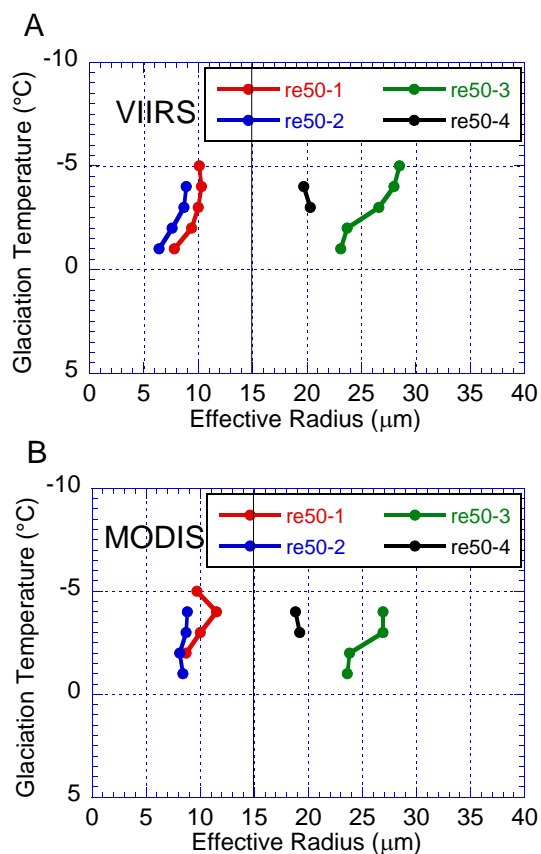


**Fig. 5.** The  $T$ – $r_e$  relations of the areas shown in Fig. 3 and denoted by white numbers, for VIIRS and MODIS. The median  $r_e$  for any given  $T$  is shown. The  $r_e$  values in the pollution tracks are much smaller than for the background clouds and are similar for both sensors. Note that VIIRS shows that  $T$  for the clouds with retrieved  $r_e$  ranges between  $-1$  and  $-5$  °C, whereas MODIS misses some of the warmest and coldest cloudy points because they are averaged out by the lower resolution.

The higher resolution data from VIIRS can supply more information and depict more detailed structure of cloud and precipitation than the previous lower resolution. Thus, the purpose of this paper is to highlight the microphysical retrievals obtained from VIIRS data and their application in the understanding of microphysical properties and cloud and precipitation formation processes while exploiting the unique capabilities the higher resolution offers. However, the standard EDR cloud products are limited to the lower VIIRS resolution of 750 m. Therefore, the first part of this study is devoted to the retrieval of a cloud mask and  $r_e$  from the 375 m imagery channels. In the following section, the method of calibration and correction of the VIIRS imager with respect to the moderate-resolution channels will be briefly given. Examples of the VIIRS-added insights that can be gained with respect to cloud composition, precipitation-forming processes and their interaction with aerosols will be

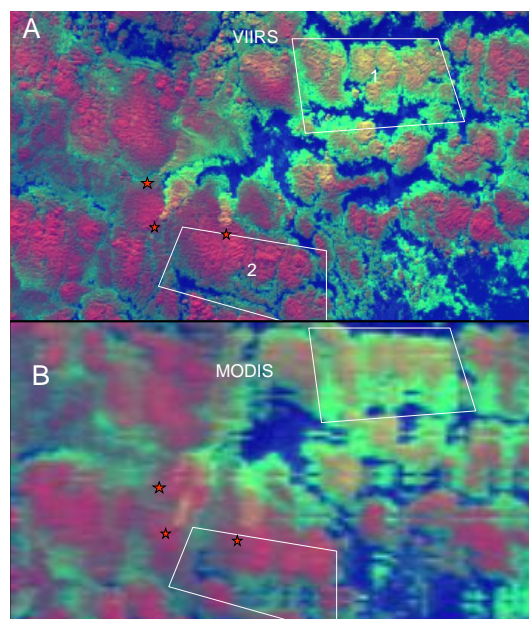


**Fig. 6.** Same as Fig. 1, but showing the three pollution point sources over the three coal power plants in the La Trobe Valley, Australia, as seen by VIIRS (04:07 UT, panel A) and MODIS (04:40 UT, panel B) overpasses on 29 April 2012, in an area of  $170 \text{ km} \times 116 \text{ km}$  centered at  $38.04^\circ \text{ S}$ ,  $146.69^\circ \text{ E}$ . The red stars are positioned below the pollution point sources, which their aerial photos are shown in Fig. 7. The pollution tracks spread northward with the southerly low-level wind and merge to the northeast and form a homogeneously polluted region that includes rectangle 1. The polluted clouds spread eastward with the westerly wind at the clouds altitude. The background clouds to the south include rectangle 2.

given and compared to MODIS are provided in Sect. 3. The summary and discussion will be given in the final section.

## 2 Using the imager for retrieving cloud drop effective radius

The VIIRS spectral bands exist in two resolutions: moderate (750 m) and imagery (375 m) at nadir. The imagery channels are available in five bands centered at 0.64, 0.865, 1.61, 3.74 and  $11.5 \mu\text{m}$  (I1 to I5 bands). The radiative accuracy of the imager is lower than the moderate resolution, but still sufficient for retrieving cloud properties. The temperature measuring accuracy ( $\text{NE}\Delta T$ ) at 210 K of the  $11.5 \mu\text{m}$  imager band is 0.8 K. The  $\text{NE}\Delta T$  at 270 K of the  $3.74 \mu\text{m}$  imager band is 0.49 K. However, in order to realize the greater accuracy of the moderate resolution, the brightness temperatures of imagery data are calibrated against the moderate resolution for each analyzed scene. This process is described in Sect. 2.1.

The first four bands exist also in the moderate resolution (M5, M7, M10 and M12), but the  $11.5 \mu\text{m}$  imager band (I5) combines most of the band widths of moderate resolution of



**Fig. 7.** The locations and aerial photos of the three coal power plants in the La Trobe Valley, Australia. The stars mark the base of the chimneys in the three zoomed-in photos. The power generation capacity is 1450 MW for Yallourn, 1600 MW for Hazelwood, and 3250 MW for Loy Yang.

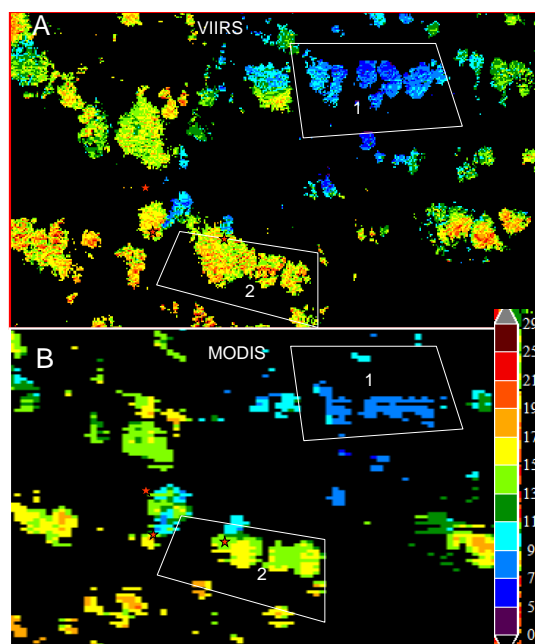


**Fig. 8.** VIIRS and MODIS retrieved effective radius for the clouds shown in Fig. 6. Only clouds with  $0.6 \mu\text{m}$  solar reflectance  $> 0.4$  are analyzed.

the  $10.8 \mu\text{m}$  and  $12.0 \mu\text{m}$  bands (M15 and M16). However, the retrieval of  $T$  and  $r_e$  requires the usage of the brightness temperature difference (BTD) between the bands of M11 and M12, which are not available separately for the imagery resolution. These bands are used for detection of optically thin clouds and for correcting  $T$  for the water vapor. Instead, it is necessary to use the BTD of the moderate resolution ( $\text{BTD}_m = T_{m11} - T_{m12}$ ). In order to obtain the BTD in im-

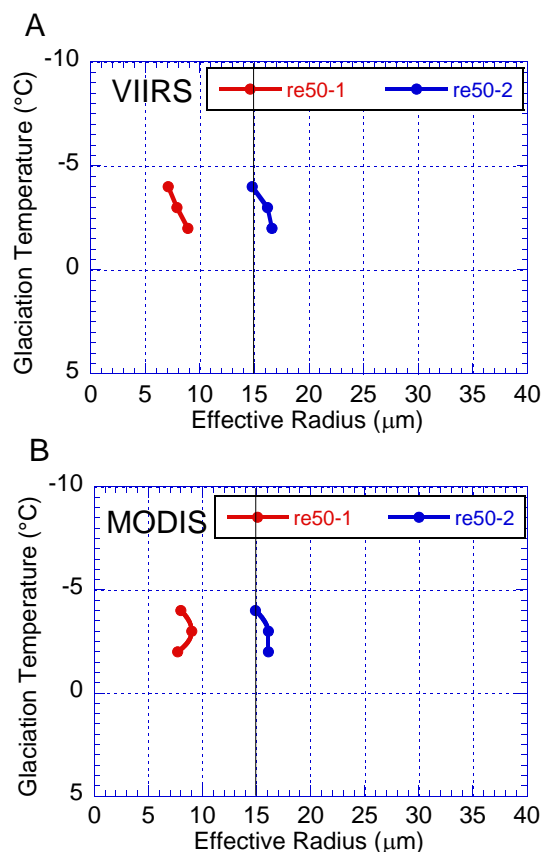


**Fig. 9.** Same as Fig. 5, but for the polluted area over the La Trobe Valley, Australia, on 29 April 2012. Line 1 (red) shows the polluted clouds with small drops that reside in rectangle 1 of Fig. 6; line 2 (blue) shows the background clouds with the larger drops that reside in rectangle 2 of Fig. 6.

agery resolution ( $\text{BTD}_h$ ), it is necessary to find out an appropriate method to get this quantity from the corresponding moderate resolution.

The retrieval of high-resolution  $3.7 \mu\text{m}$   $r_e$  is done using preferably  $3.7 \mu\text{m}$  solar reflectance, because it can inherently provide the most accurate results because water absorbs more strongly at this wavelength than any other in the solar atmospheric windows. The clouds three-dimensional effects become more dominant when retrieving smaller cloud elements, which deviate more from the plane-parallel assumption used usually for retrieval of  $r_e$  (Nakajima and King, 1990). In addition, in smaller cloud measurement volumes, more photons originate from outside the volume. Therefore, there is an inherent advantage for using more-absorbing wavelengths with shorter free paths for the photons when measuring smaller cloud volumes (Goren and Rosenfeld, 2013; Rosenfeld et al., 2004; Painemal and Zuidema, 2011). Using  $3.7 \mu\text{m}$ , we could assume a negligible effect of upwelling radiation at this wavelength from below the clouds when their visible solar reflectance ( $0.6 \mu\text{m}$ ) exceeds 0.4 over

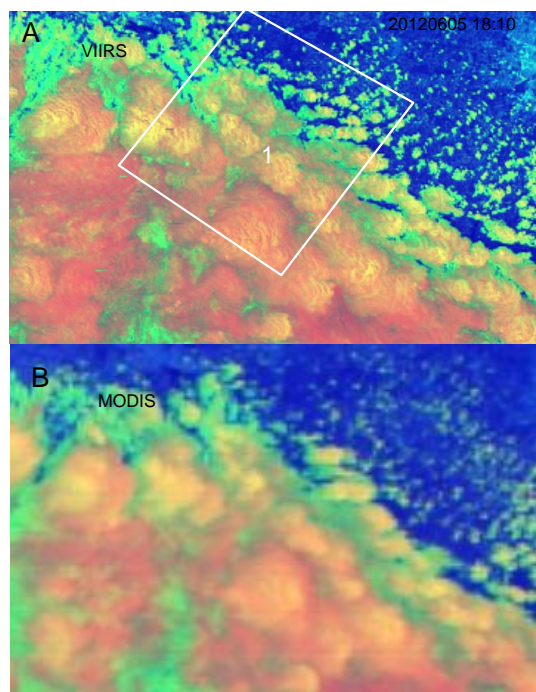


**Fig. 10.** Same as Fig. 1, but showing the regionally polluted clouds over the region of Buffalo, NY, USA, and to the south of Lake Ontario, as seen by VIIRS (18:10 UT, panel A) and MODIS (18:30 UT, panel B) overpasses on 5 June 2012, in an area of 160 km  $\times$  113 km centered at 42.74° N, 78.55° W.

land, or 0.3 over ocean, and hence greatly simplify the retrieval procedure for such clouds.

A complicating factor in retrieving  $r_e$  based on the 3.7  $\mu\text{m}$  solar reflectance is the need to separate the solar reflectance and thermal emission components at that wavelength. The solar reflectance has to be calculated from the total measured radiation after subtracting the thermal emission, which is a function of the temperature of the cloud top emitting the radiation,  $T$ . Therefore, determining  $T$  at the imagery resolution is necessary. The procedures for obtaining this are described in Sect. 2.2.

## 2.1 Dynamic calibration of 3.74 and 11.45 $\mu\text{m}$ imagery resolution data

For all pixels within a selected analysis area of 512  $\times$  512 window of the imagery bands, the overlapping 256  $\times$  256 moderate-resolution pixels are expanded to the corresponding 512  $\times$  512 pixels by the method of the nearest value sampling. The brightness temperature of cloudy pixels of the 3.74  $\mu\text{m}$  imagery ( $T_{3.7h}$ ) bands are regressed linearly to that from fully cloudy pixels of the moderate resolution ( $T_{3.7m}$ ), and the regression parameters are applied to calibrate  $T_{3.7h}$  to  $T_{3.7m}$ .

The available product of VIIRS Cloud Mask was insufficient for the objectives of calculating valid effective radius

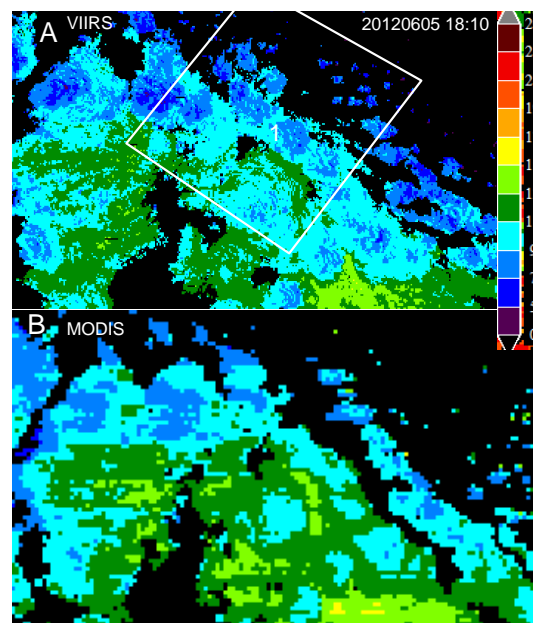


**Fig. 11.** VIIRS and MODIS retrieved  $r_e$  for the clouds shown in Fig. 10. Only clouds with 0.6  $\mu\text{m}$  solar reflectance  $> 0.4$  are analyzed.

from the imager without significant surface contamination. Instead, a cloud mask for the moderate resolution is identified as those pixels having a visible reflectance greater than a set threshold (usually 0.40) and the  $\Delta T_{11h} < 1$ . The  $\Delta T_{11h}$  is the homogeneity parameter of 11.45  $\mu\text{m}$  brightness temperature ( $T_{11h}$ ). It can be written as

$$\Delta T_{11h} = \frac{1}{4} \sum_{i=1}^4 ||T_{11hi} - \overline{T_{11h}}||,$$

where  $\overline{T_{11h}}$  is the brightness temperature of every four pixels in the imagery that reside within one moderate-resolution pixel, and  $T_{11hi}$  is their average, based on the average of absolute deviation from the mean  $T_{11h}$  within four imagery resolution pixels that reside within one moderate-resolution pixel. If  $\Delta T_{11h}$  is greater than the given threshold, a cloud edge is determined.

The same recalibration processing is carried out for pixels between the 11.45  $\mu\text{m}$  at the imagery resolution and the moderate resolution (M15) that they reside in. The regression parameters are applied to  $T_{11h}$  so that it is forced to equal on average to  $T_{11m}$ .

## 2.2 Difference of brightness temperature of cloudy pixels for imagery resolution

All the cloudy pixels within the analyzed area (usually a convective cloud cluster) are sorted by the recalibrated  $T_{11h}$ . The distributions of  $\Delta T_{11h}$  and  $\text{BTD}_m$  for each  $T_{11h}$  interval of 1  $^{\circ}\text{C}$  are calculated. The warmest  $T_{11h}$  for which a percentile



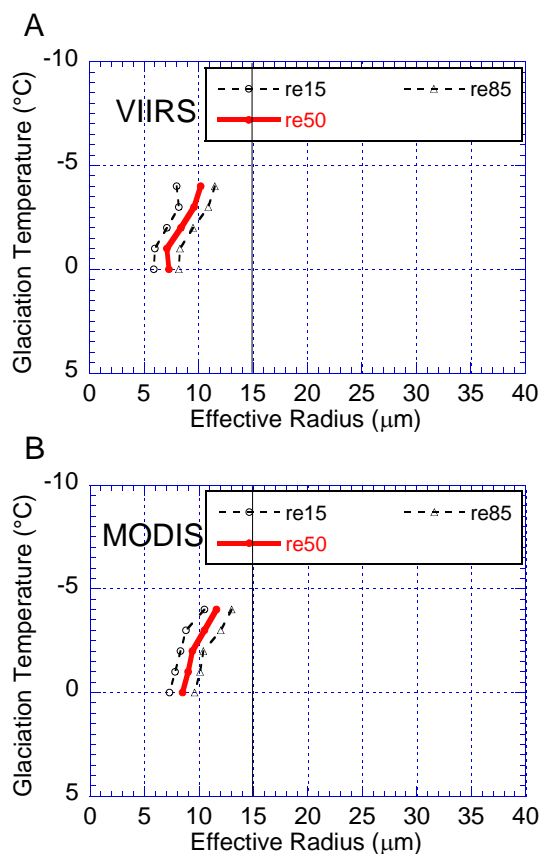


**Fig. 12.** Same as Fig. 5, but for the regionally polluted area over Buffalo, NY, USA, and to the south of Lake Ontario, on 5 June 2012. The  $T$ – $r_e$  lines are plotted for the rectangles shown in Fig. 10. The red line shows the median  $r_e$  for any given  $T$ , and the broken lines show the 15th and 85th percentiles, as indication for the spread of  $r_e$  for a given  $T$ .

$P$  of  $\Delta T_{11h} < 1$  is considered as the cloud-base temperature ( $T_{cb}$ ). The value of  $P = 30\%$  was experimentally found to match the cloud-base temperature best as inferred by radiosondes. An additional algorithm for finding a more exact cloud-base temperature is now under development, and the results will be reported separately.

The BTD of thick clouds should decrease monotonically for colder cloud tops, because the remaining vapor above the tops decreases. The value of BTD increases at colder cloud-top temperatures only if the clouds become thinner, so that more radiation is upwelling through the cloud at  $T_{11m}$  than at  $T_{12m}$  (Inoue, 1987). Therefore, in order to correct the cloud-top temperature for vapor, the following algorithm is applied:

The imagery BTD is calculated as the recalibrated  $T_{11h} - T_{12m}$ . The first quartile of the BTD for a given  $T_{11h}$  is calculated as  $BTD_4$ . The BTD is used for water vapor temperature correction. However, the appearance of a thin layer cloud above the object, for which corrected temperature due to water vapor is sought, will add to the BTD and will therefore cause an overestimated BTD vapor temperature correc-

tion. A preventive measure against this possibility is calculating  $BTD_{min}$ , which is calculated by allowing  $BTD_4$  to decrease monotonically or remain unchanged with decreasing  $T_{11h}$ , or remain unchanged if  $BTD_4$  increases for lower  $T_{11h}$ , starting from  $T_{cb}$  until the lowest  $T_{11h}$ . The monotonic decrease is enforced because any increase in  $BTD_4$  with decreasing  $T_{11h}$  can be caused only by overlying semitransparent clouds. If  $T_{11h} > T_{cb}$ , the pixel is regarded as cloud-free, and its BTD is assigned to  $BTD_m$ .

The surface temperature is calculated by  $T_{11m}$ ,  $T_{12m}$  and the solar zenith angle using the formulation of Sullivan et al. (1993). For calculating cloud surface temperature, the  $T_{11h}$  and  $BTD_4$  are used instead. Cloud surface temperature is considered invalid for calculating  $r_e$  if  $BTD_m > BTD_{min}$  by more than a user-defined value (usually  $1^\circ\text{C}$ ), indicating that the cloud is optically thin or under semitransparent clouds.

### 2.3 Retrieval of effective radius

Based on the radiation transfer model (Nakajima and King, 1990), a look-up table is established for effective radius of water cloud drop. By using the retrieved reflectance at  $3.7\ \mu\text{m}$  and geographical data supplied by the satellite,  $r_e$  is obtained via the method used by Rosenfeld and Lensky (1998). The  $r_e$  is calculated based on the  $3.7_h$  recalibrated to the  $3.7_m$  channel, the calculated cloud surface temperature, the satellite, solar azimuth and zenith angles, and the seasonal dependence of the Sun–Earth distance.

After this processing of VIIRS data, the surface temperature, the BTD and  $r_e$  for the imagery resolution can be used in the microphysical retrieval of satellite data, and  $T$ – $r_e$  relations are constructed as done by Rosenfeld and Lensky (1998).

### 3 Contrast of cloud properties reflected by VIIRS and MODIS

The pixel size of the VIIRS imagery is  $1/7$  of the MODIS pixel size at nadir, and even smaller, down to nearly  $1/20$  further away from nadir across track. The added resolution of VIIRS is expected to better resolve the small convective cloud elements of cumulus and stratocumulus clouds, both spatially and vertically. This is of great importance for applications of detecting the impacts of aerosols on clouds that ingest air from the boundary layer, because these clouds are typically small and shallow. However, a useful measurement of the  $T$ – $r_e$  relations can serve as a powerful tool for retrieving convective cloud drop number concentrations near its base and for studying cloud–aerosol interactions (Freud et al., 2011; Rosenfeld et al., 2012b). Such  $T$ – $r_e$  analysis is possible because almost all cloud drops are very small at cloud base, and the aerosols impact only in the rate of growth of  $r_e$  with increasing height or decreasing  $T$  (Rosenfeld and Lensky, 1998; Freud et al., 2011). The 375 m resolution of

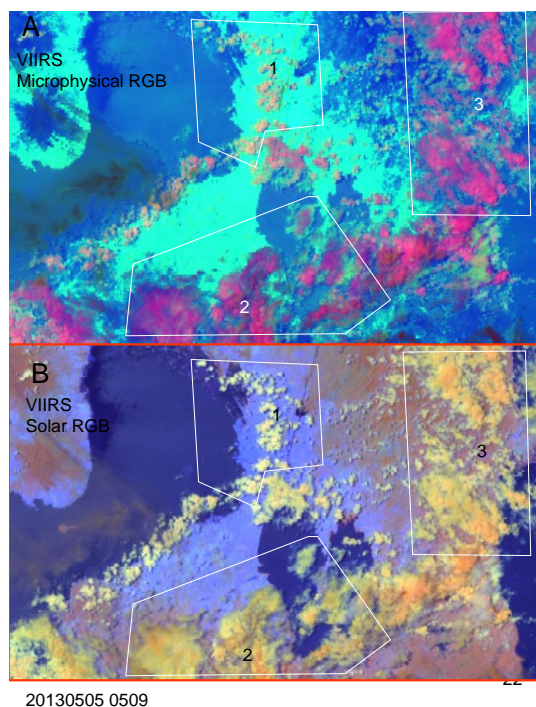


**Fig. 13.** Imagery of VIIRS overpass on 5 May 2013 05:09 UT over Manila, the Philippines. Panel (A) shows the microphysical RGB, and panel (B) shows the solar RGB, where the RGB components are modulated by the 0.8, 1.6, and 3.7  $\mu\text{m}$  solar reflectance, respectively. Panel (B) is given for a better geographic orientation while keeping some of the microphysical sensitivity in the colors of the clouds. The bright blue is the urban area. The clouds are moving from east to west (right to left). Note that in panel (A) the contrast between the clouds with small drops over the city (area 1) and the background clouds with large drops, as indicated by their reddish color. The areas of panels (A) and (B) are the same as 157 km  $\times$  122 km centered at 14.43° N, 121.13° E.

the VIIRS imager also affords an ability to resolve the impacts of local aerosol emissions such as power plants, ship stacks, vegetation fires, urban areas, dust storms, and changes in land use.

In accordance with this objective, several cases are provided to give a vivid demonstration of the improvement in the detection capability of the impacts of aerosol on cloud properties that are observed by VIIRS and MODIS. The examples include ship tracks, pollution tracks in continental stratocumulus, city or industrial pollution signatures, and tropical convection in pristine and polluted clouds and pyro-cumulonimbus (pyro-Cb). The cases were selected for the most similar satellite views (overpass time and satellite zenith angle) as possible. The images are presented with several red–green–blue (RGB) compositions, as defined in Rosenfeld and Lensky (1998). These compositions are defined in Table 1.

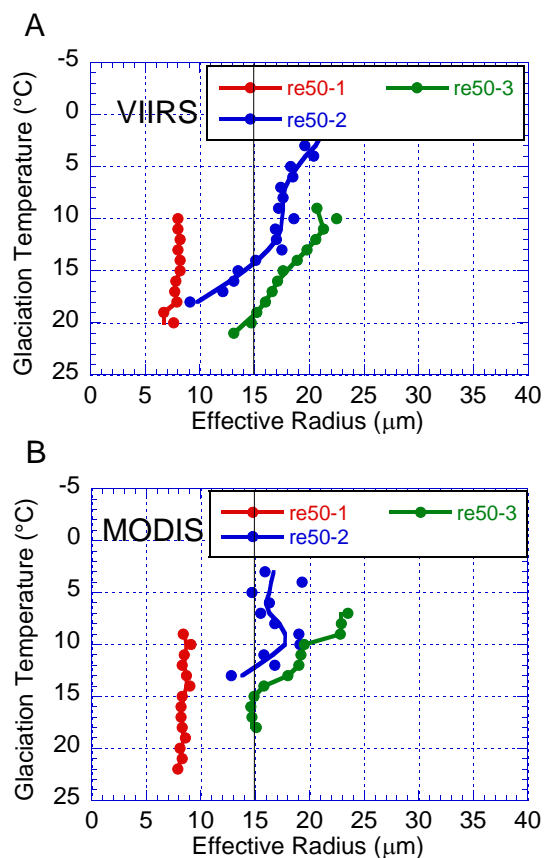


**Fig. 14.** Same as Fig. 5, but for the contrasting conditions between the polluted clouds over Manila (line 1) and the pristine background clouds (lines 2 and 3), as shown for VIIRS in Fig. 13. The MODIS image is not shown. Note the less noisy and smoother  $T-r_e$  relations for VIIRS as compared to MODIS.

**Table 1.** RGB compositions of microphysics, solar, and “natural color” schemes.

	Red	Green	Blue	Gamma
Day microphysics	0.6 $\mu\text{m}$ 0.0–1.0	3.7 $\mu\text{m}$ 0.–0.3	11 $\mu\text{m}$ 233.0–313.0	1, 1, 1
Day solar	0.8 $\mu\text{m}$ 0.0–1.0	1.6 $\mu\text{m}$ 0–0.7	3.7 $\mu\text{m}$ 0–0.6	1.7, 1.7, 2.5
Day natural	1.6 $\mu\text{m}$ 0.0–1.0	0.8 $\mu\text{m}$ 0.0–1.0	0.6 $\mu\text{m}$ 0.0–1.0	3.0, 3.0, 3.0

The “microphysical RGB” is named such because it shows the cloud microstructure. The green component is modulated by the solar reflectance of 3.7  $\mu\text{m}$ , which is roughly inversely proportional to the cloud drop effective radius, and the blue is modulated by the temperature. This provides a color scale that classifies cloud composition and temperature by its colors, as described by Rosenfeld and Lensky (1998) and Lensky and Rosenfeld (2008).



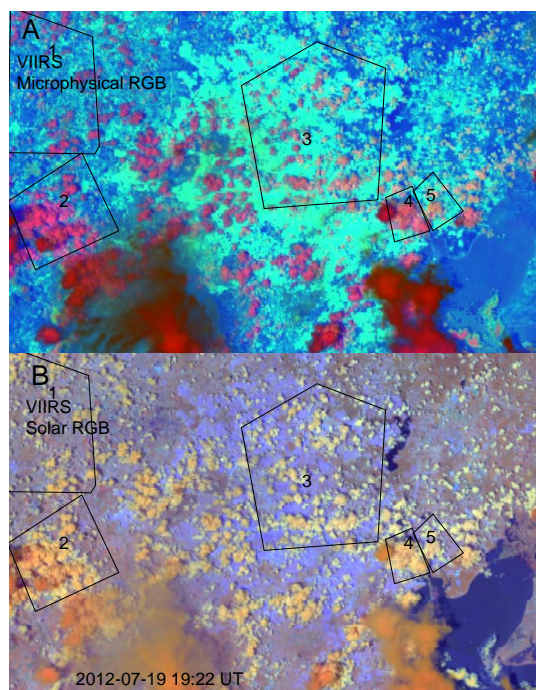


**Fig. 15.** Imagery of VIIRS overpass on 19 July 2012 19:22 UT over Houston, Texas. Panel (A) shows the microphysical RGB, and panel (B) shows the solar RGB. Note the much brighter (i.e., with smaller  $r_e$ ) clouds over the urban area compared to its surroundings. The urban area appears as the bright blue in both panels. The wind direction is from south to north (bottom to top of the image). The areas of panels (A) and (B) are the same as 198 km  $\times$  135 km centered at 29.76° N, 95.43° W.

### 3.1 Ship tracks

Ship tracks represent the best natural laboratory for observing the localized impacts of point source pollution aerosols. Figure 1 shows the microphysical RGB composite imagery of ship tracks in the northeastern Pacific Ocean. Panels a and b show the VIIRS and MODIS images for the same area within overpasses that are 20 min apart and differ in satellite zenith angle by 3°. The MODIS image covers the same area as the NPP, and the higher resolution of VIIRS is evident (Hillger et al., 2013). Here attention is focused on the added information content for understanding cloud processes. This can be done best on ship tracks that occur in such marine stratocumulus, because the cloud-top temperatures were very near 12 °C for the clouds both in and out of the ship tracks. The  $r_e$  values of the track retrieved by VIIRS and MODIS are nearly the same, with lowest values of about 10  $\mu\text{m}$ , as shown in Fig. 2. For the clouds near the track, the  $r_e$  is around 20  $\mu\text{m}$ . The flat cloud tops allowed for the effect of the ship-emitted aerosols to be resolved without the need to use  $T-r_e$  relations. The  $r_e$  of the track is considerably different from the background clouds, in line with many previous observations (Radke et al., 1989; Coakley et al., 1987; Ferek et al., 2000).

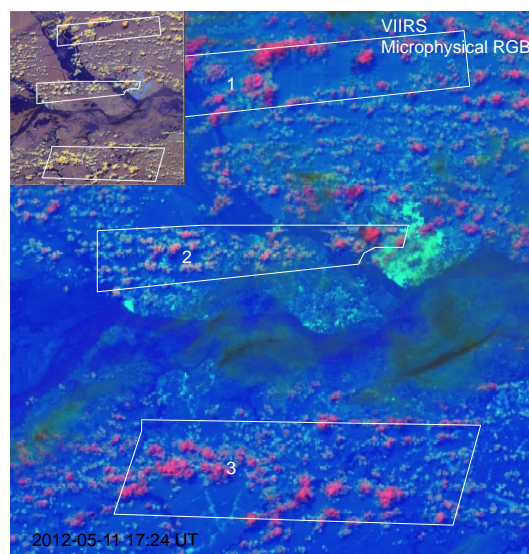


**Fig. 16.** Imagery of VIIRS overpass on 11 May 2012 17:24 UT over Manaus in the Amazon rainforest for an area of 146 km  $\times$  133 km centered at 3.19° S, 60.29° W. The color scheme is microphysical RGB. The inset in the upper left is the same area in solar RGB that better shows the surface features and the Amazon River. The city of Manaus can be seen as the bright blue area at the right edge of area 2, which marks the plume of polluted clouds, which move from east to west (right to left). The pristine background clouds are shown in areas 1 and 3.

Comparing the MODIS and VIIRS images shows that all ship tracks are evident in both images. However, details of their internal structure are more resolved by the VIIRS imager, while not discerned well by the MODIS. The details that can be resolved by VIIRS but lost in MODIS in this image are as follows:

- The head of the ship tracks are formed by very small individual clouds with much-reduced  $r_e$ , as evident by the much brighter color, that grow both through the background clouds (point 1 in Fig. 1a) and in the gaps between the background clouds (point 2). MODIS only shows a faint line as the head of the ship track.
- The young, thin ship tracks in this case fill the gaps between the background clouds (point 3), but because the gaps between the clouds are barely resolved by MODIS, this filling is not so evident by MODIS observed ship track.
- An older and wider ship track (point 4) appears as a divergent pattern of the cloud tops in VIIRS that appears to be involved in the mechanism of widening of the ship track. The microphysical texture of the ship track is, however, not resolved by MODIS.
- The intersection of an old and widely expanded ship track with a younger one (point 5) shows the relative

microphysical relations between the two. The younger ship track can be discerned superimposed on the disturbance that the old ship track has caused to the local flow and cloud microstructure as a wavy path of reduced  $r_e$ , as discerned by its brighter color. This relation is much less evident in the MODIS image.

- The  $r_e$  is retrieved for smaller clouds in VIIRS than for MODIS, because these smaller clouds fill the footprint of the VIIRS imager, but not of MODIS. This is evident in the background broken clouds, especially on the right side of Fig. 2.

### 3.2 Pollution track

The closest phenomenon to ship tracks over land is pollution tracks from stacks of coal power plants and other pollution point sources. The ability of the VIIRS imager to detect such a pollution track is shown in this case. A pollution track caused by a coal power plant in Australia was clearly detected by both VIIRS and MODIS (see Fig. 3). In fact, looking at origination coordinates of the head of the pollution track (shown in Fig. 3 with a red star) with Google Earth revealed the coal power plant shown in Fig. 4. Similar pollution tracks over Australia were previously documented by Rosenfeld (2000). The tracks are evident in the microphysical RGB composite imagery (represented by areas 1 and 2 in Fig. 3) by the yellow color of the clouds, which reflects their small  $r_e \sim 10 \mu\text{m}$ . The background clouds (represented by areas 3 and 4 in Fig. 3) are shown as red, which reflects their large  $r_e > 20 \mu\text{m}$ . These clouds are deeper than the marine stratocumulus in the case of the ship tracks. This allows constructing  $T-r_e$  relations for these clouds (Fig. 5). According to the VIIRS  $T-r_e$  in Fig. 5 the clouds extend vertically between 0 and  $-5^\circ\text{C}$  isotherms. VIIRS and MODIS retrieved similar microphysical properties in and out of the pollution track. The  $r_e$  of clouds in the pollution track all ranges from 5 to  $10 \mu\text{m}$  from NPP and MODIS, while the  $r_e$  of clouds out of the pollution track are  $20\text{--}30 \mu\text{m}$  and  $17\text{--}27 \mu\text{m}$  for NPP and MODIS, respectively.

Comparing the MODIS and VIIRS images shows that, as with the ship tracks, the pollution track was evident in both images, but the fine structure that is seen in VIIRS (Fig. 3b) gets lost in the MODIS image (Fig. 3e). This is most evident by a tiny pollution track that seems to have originated from a fire that appears as the hot spot marked by point 5 in the magnified inset shown as Fig. 3c. The MODIS view of the same area is shown in Fig. 3f. The hot spot is not resolved there, and the individual yellow small clouds that are evident in the VIIRS imager are blurred into a faintly brighter area in the MODIS image. The finer detail of VIIRS is also evident in Fig. 5, as MODIS missed some of the warmest and coldest cloudy points because they are averaged out by its lower resolution.

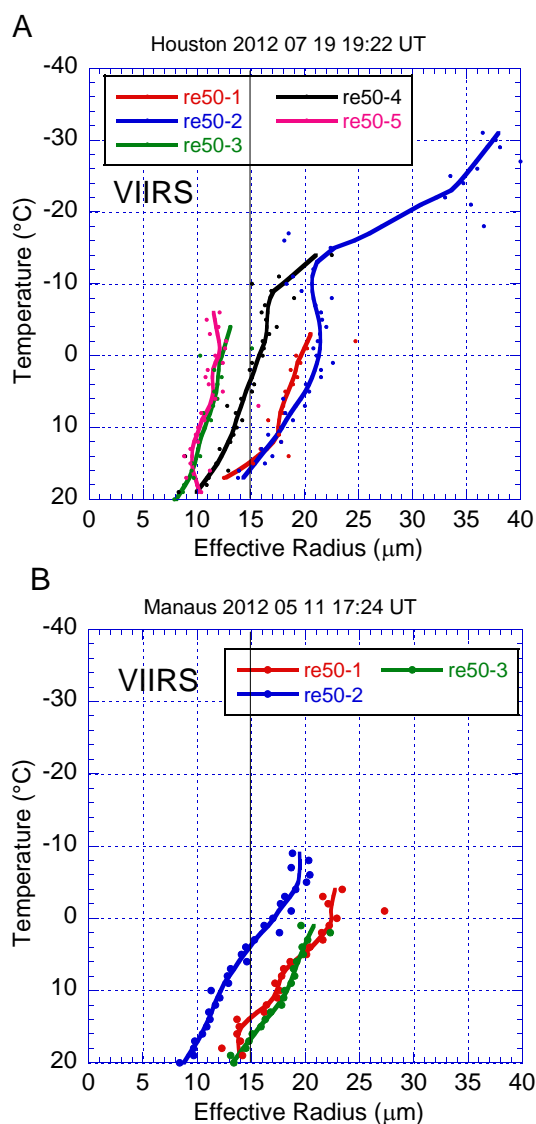


**Fig. 17.** Same as Fig. 5, but for the contrasting conditions between the polluted clouds. Panel (A): urban polluted clouds with reduced  $r_e$  over Houston, Texas (lines 3 and 5), compared with background clouds to the west and NW of the city (lines 1 and 2), represent the areas shown in Fig. 15. Panel (B): the  $T-r_e$  of the clouds pollution plume of Manaus in the Amazon is shown by line 2, whereas lines 1 and 3 show the background pristine clouds that represent the areas shown in Fig. 16.

### 3.3 Merging of pollution tracks into regional pollution

The most conspicuous pollution tracks that spread into regional pollution were shown over the La Trobe Valley to the east of Melbourne, Australia, where a cluster of coal power plants were built near open-pit coal mines (Rosenfeld, 2000). The attribution of the satellite-observed reduced  $r_e$  in the region to the emissions of the power plants was disputed by Ayers (2005) and rebutted by Rosenfeld et al. (2006), who

**Table 2.** Cloud samples in this study.

Fig. no.	Date	Time		AN	Lat.	Long.	Location	CT	CC	Feature	AOD	Satz		$T_{\text{base}}$		$T_{14}$		$T_{\text{g}}$		$T_{\text{top}}$		
		V	A									V	A	V	A	V	A	V	A			
1	15/07/2012	22:20	22:40	1	40.76	-139.77	Eastern Pacific	Sc	M	ship track		21	25	11	12					12	12	
				2	40.85	-139.79	Eastern Pacific	Sc	M	ship track		21	25	11	12					12	12	
3	06/06/2012	03:56	04:05	1	-33.03	149.79	Australia	Sc	C	polluted track		22	16	-1	-1					-5	-5	
				2	-32.47	149.00	Australia	Sc	C	polluted track		18	11	0	4					-4	-4	
				3	-33.05	150.39	Australia	Sc	C	clean		25	19	0	2	0	2			-5	-4	
				4	-33.32	149.90	Australia	Sc	C	clean		22	15	-2	-2	-2	-3			-4	-4	
6	29/04/2012	04:07	04:40	1	-37.86	146.97	Australia	Sc	C	polluted track		15	45	-2	-2					-4	-4	
				2	-38.34	146.72	Australia	Sc	C	clean		13	43	-2	-2	-2	-2			-4	-4	
10	05/06/2012	18:10	18:30	1	42.91	-78.60	New York	Sc	C	polluted	0.14	12	23	2	12					-5	-5	
13	05/05/2013	05:09	05:25	1	14.82	121.59	Manila	Cu	M	clean	0.14	3	10	20	23	19	15			8	2	
				2	14.61	121.06	Manila	Cu	C	polluted	0.14	3	10	18	16	13	11			-3	3	
				3	14.12	120.89	Manila	Cu	C	clean	0.22	7	15	21	21	19	18			7	7	
				1	29.98	-96.22	Houston	Cu	C	clean	0.14	-5		17		15				-3		
				2	29.59	-95.98	Houston	Cu	C	clean	0.14	-4		17		15		-18			-31	
15	19/07/2012	19:22		3	29.86	-95.22	Houston	Cu	C	polluted	0.14	3		20		-1				-4		
				4	29.72	-95.03	Houston	Cu	C	polluted	0.14	3		19		4				-14		
				5	29.78	-100.00	Houston	Cu	C	polluted		4		19						-6		
				1	-2.73	-60.31	Manaus	Cu	C	clean	0.1	5		18		13				-4		
				2	-3.13	-60.35	Manaus	Cu	C	polluted	0.1	4		20		6				-8		
16	11/05/2012	17:24		3	-3.60	-60.12	Manaus	Cu	C	clean	0.1	5		20		16				1		
				1	-4.90	127.89	Indonesia	Cb	M	clean	0.1	10	-8.5	22	22	15	17	-20	-14	-75	-64	
				1	-26.07	146.83	Australia	Cb	C	clean		17	7	17	22	-1	-2	-18	-16	-64	-60	
19	15/02/2012	03:59	04:05	1	-6.31	106.27	Jakarta	Cu	C	polluted	0.98	22	22	-4								
20	29/09/2012	06:32		1	28.61	115.93	China	Cb	C	polluted	0.6	33	22			-15		-20				-37
21	12/07/2013	05:37	05:20	1	65.78	105.11	Siberia	Cb	C	clean	0.62	12	2	9	21	-18	-20	-40	-40	-67	-62	
				2	65.25	107.37	Siberia	Cb	C	firestorm	0.62	18	9	22	23			-40	-40	-61	-59	
				3	65.73	107.31	Siberia	Cu	C	clean	0.62	19	10	10	20					-24	-17	
				4	65.75	108.31	Siberia	Cu	C	firestorm	0.54	22	14	22	23					-13	-17	

Fig. no.: figure number in the context; Time: satellite overpass time, in which V and A stand for imagers of VIIRS and AQUA, and same hereinafter; AN: number of area selected in the figure; Lat. and Long.: central latitude and longitude of selected area; Location: country or city where clouds are located; CT: type of cloud classification; Sc: stratocumulus; Cu: cumulus; Cb: cumulonimbus; CC: general cloud properties in which M and C stands for maritime or continental cloud, respectively; Feature: cloud feature or impact by pollution or clean cloud for comparing with the polluted cloud; AOD: aerosol optical depth from MODIS product; Satz: satellite zenith angle;  $T_{\text{base}}$ : temperature of cloud base;  $T_{14}$ : temperature of  $r_e$  reaching 14  $\mu\text{m}$ , initiation of precipitation;  $T_{\text{top}}$ : temperature of cloud top;  $T_{\text{g}}$  is the glaciation temperature.

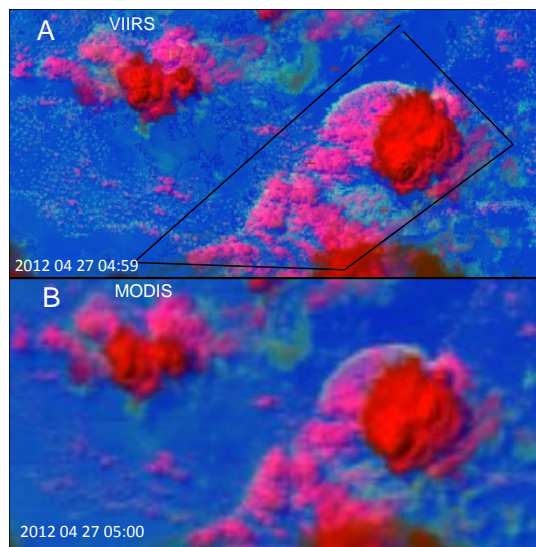


**Fig. 18.** Pristine oceanic deep convection, as seen by the VIIRS (A) and MODIS (B) overpass on 27 April 2012 over the Banda Sea near Indonesia for an area of 140 km  $\times$  101 km centered at 4.90° S, 127.72° E. The color scheme is microphysical RGB. Note the bright rim of the gust front, caused by the shallowness of the clouds there, which in turn causes the cloud drops to be smaller.

meticulously analyzed the cloud motions and composition with respect to the location of the emission sources. The ad-

vent of VIIRS readily resolves this argument by showing the individual plumes of polluted clouds that originate from each of the stacks of the power plant, shown here in Figs. 6 and 7.

Figure 6 shows the three distinct bubbling cloud tops with very small  $r_e$  immediately above the stacks of three major coal power plants in the La Trobe Valley, shown in Fig. 7. The conspicuous reduction in  $r_e$  from a background of  $\sim 15 \mu\text{m}$  to about 7  $\mu\text{m}$  just over the smoke stacks is shown quantitatively in Fig. 8. The  $T-r_e$  values of the polluted and background clouds are captured similarly by both MODIS and VIIRS, as shown in Fig. 9; this is likely owing to the large horizontal dimensions of these stratocumulus clouds, as evident in Fig. 6, and is in contrast to the highly localized pollution signatures within the clouds over the stacks of the power plants. These small, bubbling, polluted clouds are not sufficiently resolved by MODIS.

The pollution tracks are blowing northward with the 10 kn southerly winds at the stack height according to the Melbourne sounding. The surface wind was WSW, along the La Trobe valley, probably due to the channeling effect of the 1000 m high Baw Baw Plateau to its north. The low-level winds likely carried part of the pollution eastward, extending the area of polluted clouds to that direction.

### 3.4 Regionally polluted clouds

The previous cases of ship tracks and pollution tracks were observed in generally pristine areas such as the middle of



the ocean and the sparsely populated continent of Australia, where the pollution is a perturbation with respect to the background. However, in the middle of densely populated areas such as western Europe and North America, the composition of most clouds is in effect similar to those in the pollution tracks. An example is given here from the region of Buffalo, NY, USA, and to the south of Lake Ontario, shown as Fig. 10. On 5 June 2012 the region was partly covered by stratocumulus clouds that had large areas of  $r_e < 10 \mu\text{m}$ , as evident in Fig. 11. In these nearly homogeneous conditions and widespread stratocumulus clouds, MODIS and VIIRS provide similar information about the clouds, although finer details are visible with the VIIRS imager.

### 3.5 Urban air pollution in tropical cumulus clouds

Rosenfeld and Lensky (1998) showed a case of urban air pollution suppressing warm rain in Manila using AVHRR data. Here we revisit this location with VIIRS, shown in Fig. 13. The background clouds in areas 1 and 3 of Fig. 13 have large drops that exceed the  $14 \mu\text{m}$  rain threshold well below their tops, thus appearing to be producing warm rain showers (Fig. 14). However,  $r_e$  in the clouds over the urban area remains well below  $10 \mu\text{m}$ , thus precluding the possibility of rain showers from these clouds. Because some of the clouds are small, the  $T-r_e$  relations as retrieved by MODIS are noisier than that of VIIRS, as evident in Fig. 14.

Similar effects were observed in deeper convective clouds in southerly flow over Houston, Texas, USA, and in the near vicinity (Fig. 15). The Houston pollution produced a plume of polluted clouds with a decreased  $r_e$  over and downwind of the urban area, shown in area 3 of Fig. 15. Clouds were affected similarly by the pollution plume of Manaus in the Amazon, as shown in area 2 of Fig. 16. The  $T-r_e$  plots are shown in Fig. 17. The pollution in Houston, at least in part, appears to originate from a large refinery at area 3 of Fig. 15, which is associated with a sharp decrease of  $r_e$  there, as shown by contrasting the lines 5 and 6 in Fig. 17a. The pollution plume of Manaus produced a conspicuous decrease of  $> 5 \mu\text{m}$  in  $r_e$  from similar values to the north and south of the plume, as shown in Fig. 17b.

### 3.6 Deep tropical convection – from pristine marine to highly polluted

Deep tropical convection is characterized by a very warm cloud base ( $> 20^\circ\text{C}$ ) and very cold cloud tops, well below the homogeneous ice nucleation temperature of  $-38^\circ\text{C}$ . The large vertical distance from cloud base to the  $0^\circ\text{C}$  isotherm as well as the large amount of condensed cloud water typically cause these clouds to precipitate much of their water as warm rain, despite having a considerable part of their volume well above the freezing level. Here we present the way in which VIIRS observes the vertical microphysical profiles of pristine clouds over ocean (Fig. 18), pristine clouds over

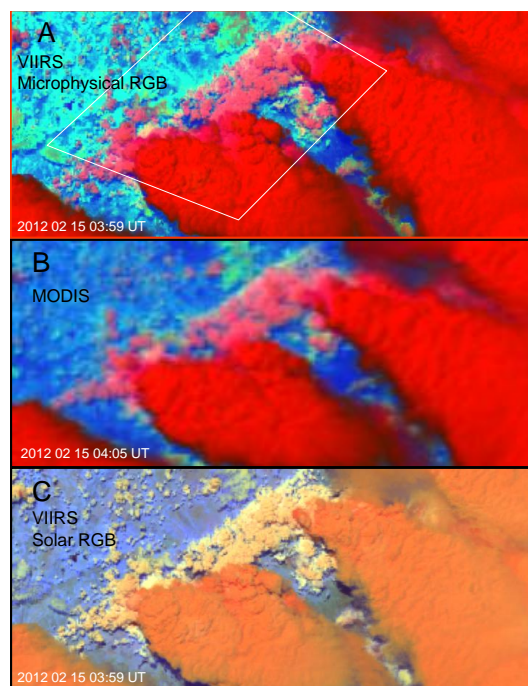


**Fig. 19.** Pristine deep convection, as seen by VIIRS (A) and MODIS (B) overpasses on 15 February 2012 over eastern Australia for an area of  $155 \text{ km} \times 109 \text{ km}$  centered at  $26.13^\circ \text{ S}$ ,  $147.02^\circ \text{ E}$ . Panels (A) and (B) are shown with the microphysical RGB and panel (C) again shows VIIRS image with the solar RGB.

land (Fig. 19), polluted clouds by diluted smoke from forest fires over Indonesia (Fig. 20), and heavily polluted clouds by the thick haze over southern China (Fig. 21). Some of the cases are compared with MODIS. The  $T-r_e$  relations of all these cases are shown in Fig. 22. This series of cases shows a systematic decrease of  $r_e$  and an increase of height where  $r_e$  exceeds  $14 \mu\text{m}$  from the pristine marine clouds to the continental pristine clouds, and to smoky and industrially polluted clouds.

The  $r_e$  in the pristine marine clouds increases very quickly with height (or with decreasing  $T$ ) until reaching a saturation value of  $\sim 22 \mu\text{m}$  at  $T < 10^\circ\text{C}$ . This marks the “rain-out zone”, where the growth of  $r_e$  at cloud top by coalescence is balanced by precipitation of the largest drops to below the satellite measurement depth of  $\sim 100 \text{ m}$  (Rosenfeld and Lensky, 1998). Comparison of VIIRS and MODIS shows that both sensors captured the main features of the deep marine convection. However, the difference in resolving the fine detail is insightful, for example, in the fine detail of the gust front that the tropical shower produced: its brighter edge indicates smaller  $r_e$ , which manifests the thinning of the cloud depth towards the leading edge of the gust front. The MODIS retrieved  $T-r_e$  (Fig. 22b) is noisier than for VIIRS (Fig. 22a). MODIS was only slightly noisier than VIIRS for the pristine continental clouds (Fig. 22c and d).

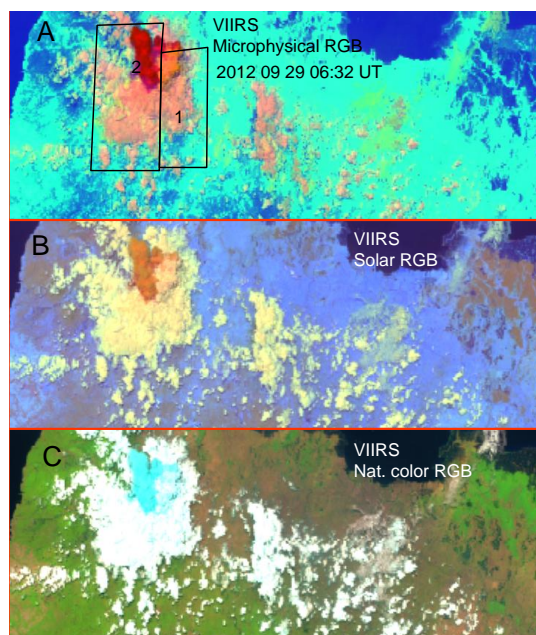


**Fig. 20.** Deep convection in smoky air over west Java, as seen by the VIIRS overpass on 29 September 2012, 06:32 UT, in an area of  $178 \text{ km} \times 78 \text{ km}$  centered at  $6.29^\circ \text{ S}$ ,  $106.55^\circ \text{ E}$ . The clouds developed in diluted smoke that was transported from forest fires in Sumatra. Note that area 1 includes a growing cloud with top temperatures reaching  $-32^\circ \text{ C}$  and yet is not glaciated. Area 2 includes an older cloud top that is glaciating between  $-10$  and  $-20^\circ \text{ C}$  (see Fig. 22e).

In general, it appears that the  $T-r_e$  vary much less below the height of initiation of precipitation or glaciation than above it, which is because the  $T-r_e$  relations below that height are dominated by the aerosols, whereas the rate of development of rain and ice hydrometeors above that height depends mainly on the updraft speed (Rosenfeld et al., 2008). This principle is evident in the case of clouds that grow in smoky atmosphere in western Java (Fig. 20). The clouds remain composed of small drops up to  $T = -5^\circ \text{ C}$ , where  $r_e$  reaches  $14 \mu\text{m}$  (Fig. 22e). The cloud top in area 1 appears to be growing vigorously based on its bubbly texture, which is seen best in panel b for Fig. 20. It remains with  $r_e \leq 16 \mu\text{m}$  down to  $T = -32^\circ \text{ C}$ , indicating a composition of mainly supercooled water cloud. The adjacent higher and seemingly older cloud tower in area 2 appears already glaciated by its smoother texture and much larger indicated  $r_e$  for the same  $T$ , as well as its blue coloration in panel c of Fig. 20, because the  $1.6 \mu\text{m}$  channel is absorbed much more strongly by ice than by water.

Figure 21 shows deep tropical convective clouds developing within an area of visible pollution haze, which was detected by MODIS Aqua as aerosol optical depth of  $\sim 0.75$ . The clouds that developed in this haze kept  $r_e < 14 \mu\text{m}$  well above the  $0^\circ \text{ C}$  isotherm level, until an abrupt increase indicated the onset of glaciation (Fig. 22f). Although only one

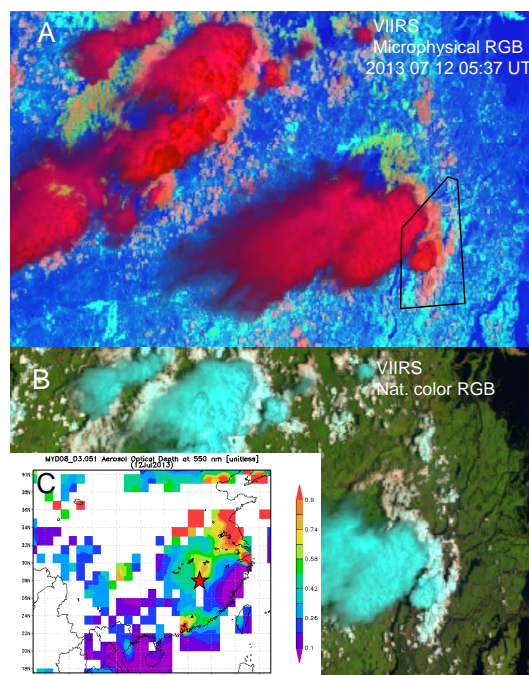


**Fig. 21.** Deep convection in haze of air pollution over southeast China, as seen by the VIIRS overpasses on 12 July 2013 05:37 UT in an area of  $200 \text{ km} \times 106 \text{ km}$  centered at  $28.74^\circ \text{ N}$ ,  $115.32^\circ \text{ E}$ . The pollution haze is shown in panel (C) as the MODIS retrieved map of aerosol optical depth (AOD). The red star shows the location of the cloud marked by the rectangle in panel (A); it is located in an area with  $\text{AOD} = 0.75$ .

cloud is shown here, this feature was repeatedly observed in all the hazy cases that were examined over China. This interpretation is in line with the results of the MODIS-based study showing that the heavy air pollution in China keeps the  $r_e$  small, but glaciates the clouds at  $\sim -20^\circ \text{ C}$  (Rosenfeld et al., 2011).

### 3.7 Pyro-Cb

The most extreme form of aerosols effect on clouds occur when a cloud directly ingests the smoke and heat from an ongoing fire. This causes a reduction in the  $r_e$  to extremely low values that can extend to great heights, which then suppresses both warm and ice precipitation processes. The  $r_e$  is so low because the heat from the fire produces very strong updrafts that then nucleate very large number concentrations of the smoke aerosols. A previous study compared pyro-Cb and naturally occurring adjacent clouds, showing that the pyro-Cb had much reduced  $r_e$  both below and above the homogeneous ice nucleation isotherm level of  $-38^\circ \text{ C}$  (Rosenfeld et al., 2007). A similar situation is analyzed and shown in Fig. 23, where pyro-Cb and naturally occurring Cb coexisted. The higher resolution of VIIRS revealed the pyro-Cb by the boiling appearance of the yellow (supercooled water) part of

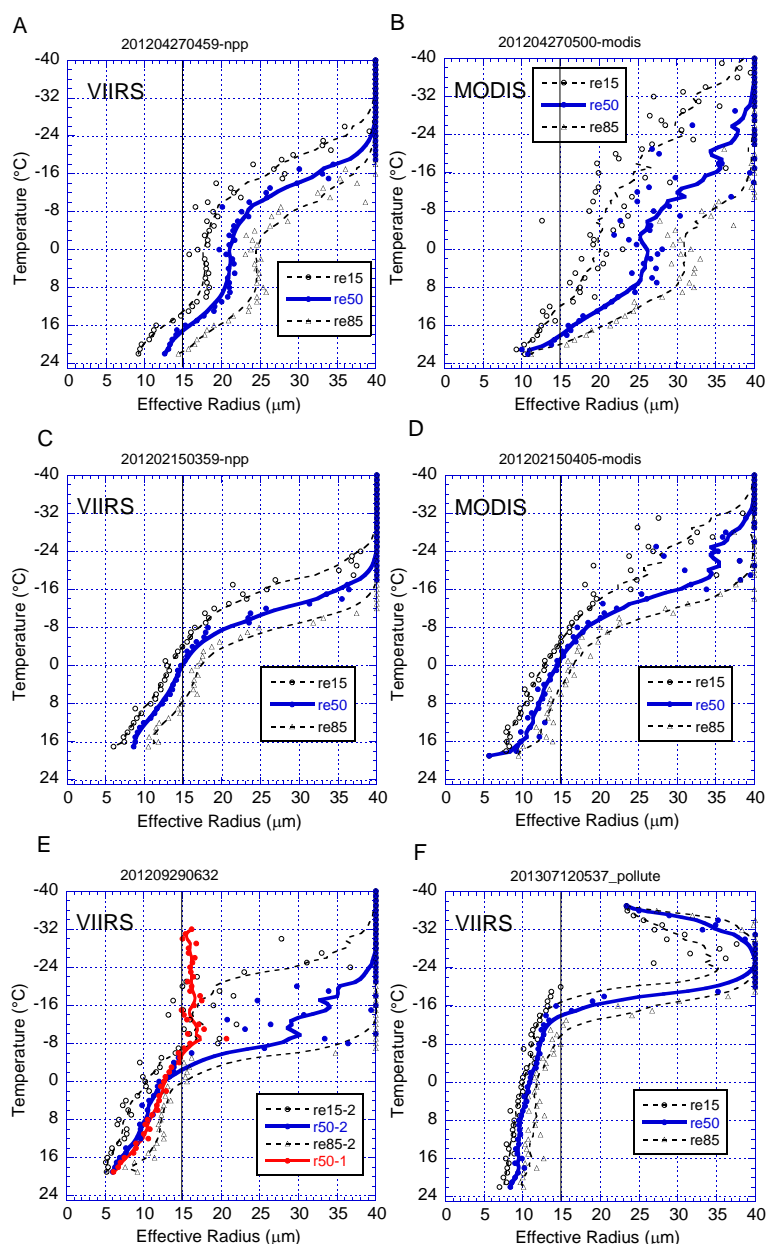


**Fig. 22.** The  $T-r_e$  relations for deep tropical convective clouds under various aerosol conditions. Shown are the 15th percentile, the median, and 85th percentiles of the  $r_e$  for any given  $T$ . Panels (A) and (B): for marine pristine marine clouds as measured by VIIRS and MODIS, respectively, shown in Fig. 18. Note the flattening of  $r_e$  at  $\sim 22 \mu\text{m}$  between 8 and  $-7^\circ\text{C}$ , which is indicative of the rainout zone; (B) and (C): pristine continental clouds over SE Australia for VIIRS and MODIS, respectively, shown in Fig. 19; (E): growing (line 1) and maturing (line 2) convective elements in smoky air in west Java, shown in Fig. 20; (F): growing convective clouds in haze of industrial pollution in SE China, shown in Fig. 21.

the cloud in panel c. These features are lost in the lower microphysical resolution of MODIS, as evident in panel f.

The VIIRS-retrieved  $T-r_e$  relation of the lower part of the pyro-Cb (line 2 in Fig. 24a) coincided with that of the smoky clouds shown as line 4. This means that the reduced  $r_e$  of the pyro-Cb was contributed mainly from the added smoke aerosols, and not to a significant extent from enhanced up-

draft speeds caused by the heat of the fire. This kind of inference is not possible through use of the MODIS-based  $T-r_e$ , because the lower parts increased anomalously, probably due to contamination from the smoke and/or partial pixel filling. At the upper parts of the clouds, above the  $-20^\circ\text{C}$  isotherm level, the  $T-r_e$  of MODIS and VIIRS were quite similar,



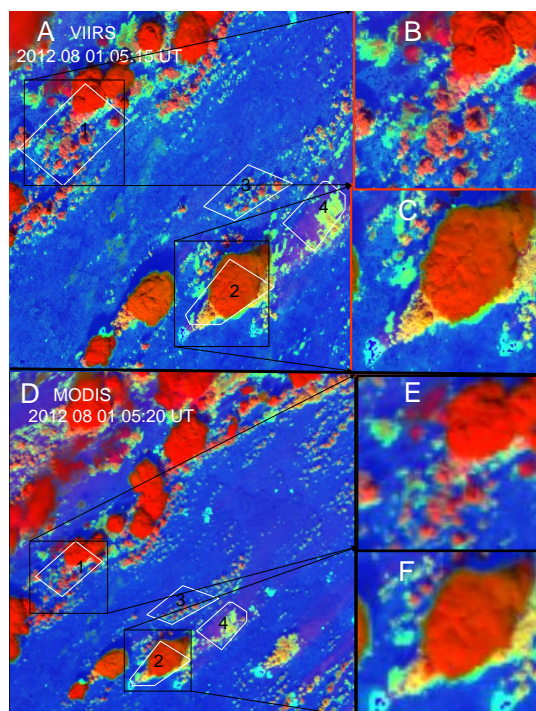


**Fig. 23.** Comparison between continental deep convection and pyro-Cb, as seen by VIIRS and MODIS. The data are from 1 August 2012 over eastern Siberia in an area of  $306\text{ km} \times 289\text{ km}$  centered at  $66.19^\circ\text{ N}$ ,  $107.05^\circ\text{ E}$ . VIIRS is shown in panels (A–C), and the analysis is repeated for MODIS in panels (D–F). Areas 1 and 3 contain Cb clouds, which are magnified to full-resolution VIIRS in panel (B) in an area of  $61\text{ km} \times 62\text{ km}$  centered at  $65.69^\circ\text{ N}$ ,  $105.29^\circ\text{ E}$  and panel (C) in an area of  $58\text{ km} \times 56\text{ km}$  centered at  $65.30^\circ\text{ N}$ ,  $107.37^\circ\text{ E}$ . The cloud in panel 3 is a pyro-Cb, which ingests the smoke and heat from the fire that appears as a light-blue area just upstream of the pointed edge of the cloud. Cumulus convection is also compared in areas 2 and 4, with area 4 being affected by the smoke from the nearby fires. The smoky clouds are visibly brighter in this microphysical RGB because of the much smaller cloud drops. The color becomes completely red when the clouds glaciate. This is quantified in the  $T-r_e$  relations shown in Fig. 24.

probably because the cloud elements at these heights were sufficiently large to match the lower resolution of MODIS.

Finally, the  $T-r_e$  relations from all the cases of the deep convective clouds are shown together in Fig. 25. The successive decrease in  $r_e$  for the same  $T$  for situations with more aerosols is clearly evident. This is coupled with the greater height and lower  $T$  to which the cloud has to grow in order to having  $r_e > 14\text{ }\mu\text{m}$  with the added aerosols.

#### 4 Discussion and summary

The 375 m resolution of the NPP/VIIRS was applied to applications of cloud microstructure. It was compared to MODIS and shown to have very similar retrieved cloud properties

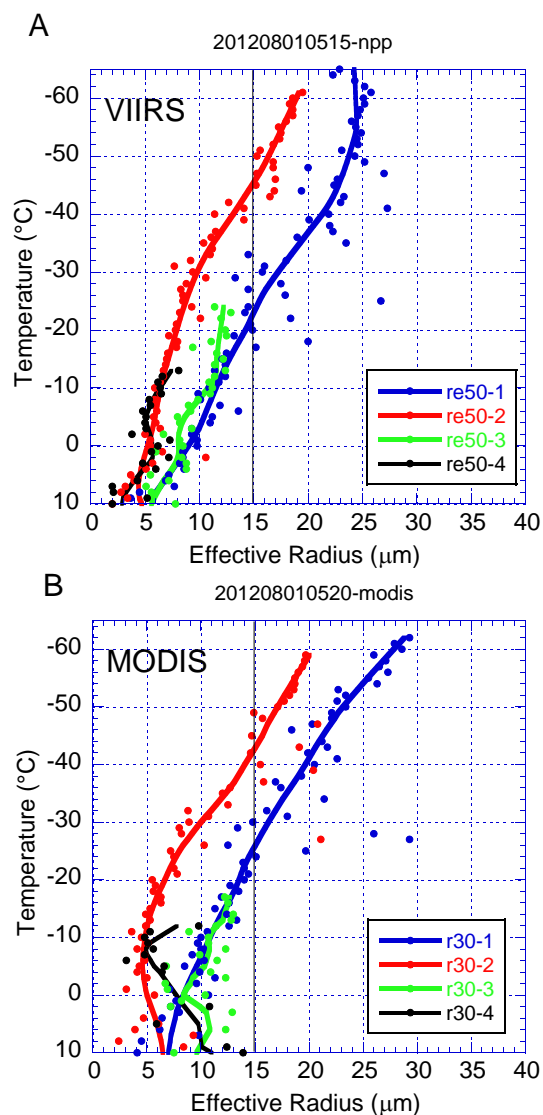


**Fig. 24.** Comparison between the  $T-r_e$  relations of continental deep convection and pyro-Cb, as seen by VIIRS and MODIS, for the case shown in Fig. 23. The red line is from a pyro-Cb; the black line is from Cu clouds that develop in smoke from adjacent fire; the blue and green lines are from Cb and Cu clouds that are not affected by the smoke. The lower parts of the MODIS retrieved  $r_e$  increased anomalously in most of the clouds, probably due to contamination from the smoke and partial pixel filling. This was not a problem in VIIRS.

for clouds with spatial homogeneity larger than the 1000 m scale of the MODIS footprint. The retrieved properties of small convective elements appeared more physically consistent with the known behavior of such clouds for VIIRS than for MODIS. The improved spatial resolution afforded the resolution of features that could not be seen until now, such as pin-pointing the reduced cloud drop effective radius directly above the stacks of coal power stations, and the fine structure of ship tracks' initiation and subsequent expansion.

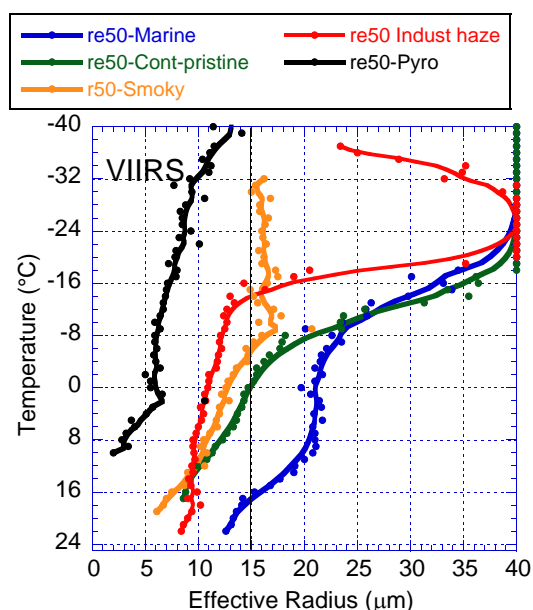


**Fig. 25.** The  $T$ – $r_e$  relations of all the types of deep convective cloud in this study.

The application of the high resolution was applied here to elucidate cloud–aerosol interactions in various cloud types and environments. A systematic VIIRS high-resolution analysis of shallow to deep clouds in the most pristine to the most polluted environments was performed and compared when possible with MODIS.

The examples include the following:

- Ship tracks in pristine broken marine stratocumulus. Features that were previously unresolved are seen in the individual rising plume of the smoky air and clouds that form the head of the ship track, as well as the expansion streaks of the track after it is formed.
- Pollution track in pristine continental stratocumulus. Three examples are provided; these demonstrated the fine detail that can be resolved by VIIRS, as in the case of the ship tracks.
- Urban pollution signatures in cumulus convective clouds. Three examples are shown with clouds in the urban plume from Houston, Manila, and Manaus, composed of significantly reduced cloud drops that suppress warm rain, as indicated by reducing to  $r_e$  below the rain initiation threshold of 14  $\mu\text{m}$ .
- Deep tropical Cb clouds in pristine air mass. Two examples are shown, one over ocean and one over land. VIIRS can resolve the fine details better than MODIS. This is manifested in the fidelity of the microphysical retrievals and is evident in the spread of the  $T$ – $r_e$  relations being smaller for VIIRS than MODIS, in this

as well as in all the other examples. A manifestation of that is a clearer identification of the warm rain or rainout signature, where the  $r_e$  saturates with increasing cloud to height until ice starts developing. VIIRS also identifies the fine detail of the gust front that the tropical shower produced, including the reduction of the cloud drops near the leading edge, where the cloud depth is thinning.

- Deep tropical convective clouds in polluted atmospheres. Two examples are given. The first one is from a developing Cb in western Java in smoke that came from forest fires in Sumatra. The growing convective element could be identified to remain composed of supercooled drops down to a temperature of  $-32^\circ\text{C}$ . An adjacent older cloud tower was already glaciated. Similar growing towers of deep tropical convection in the heavy pollution haze over southeast China showed that the haze kept the cloud drops very small ( $< 13 \mu\text{m}$ ) down to the  $-20^\circ\text{C}$  isotherm level, where it glaciated, probably due to the ice nuclei content of the Chinese urban and industrial air pollution (Rosenfeld et al., 2011).
- Pyro-Cb, i.e., a cloud that feeds directly from the heat and smoke of an intense fire. An example of unperturbed and nearby pyro-Cb over eastern Siberia is presented. The pyro-Cb had much smaller  $r_e$  for the same  $T$  of the unperturbed continental clouds, which already had a rather small  $r_e$ , which reached 14  $\mu\text{m}$  only at the  $-20^\circ\text{C}$  isotherm. VIIRS shows the fine detail of the billowing clouds that occur directly over the fire, delivering the impression of their intense bubbling vigor, whereas the MODIS 1 km microphysical resolution misses this kind of detail.

In summary, VIIRS provides sounder physical interpretation and more detailed information for cloud information than MODIS, especially in the initial stage of cloud formation. VIIRS can supply significantly more fully cloudy pixels in the small boundary layer convective elements, reduced uncertainty in determination the cloud base, and a better cloud mask by using the homogeneity parameter ( $\Delta T_{11h}$ ) for minimizing surface effects. It also can be used to obtain more detailed structure of cloud tops, which, in turn, allows for a better quantification of the cloud–aerosol interactions and impacts on precipitation-forming processes.

*Acknowledgements.* This research was supported by the China Special Fund for Meteorological Research in the Public Interest (GYHY201306005) and the National Basic Program of China (973 Program, 2013CB955800). We are grateful to the supports from Shaanxi Administration of Foreign Expert Affairs. The authors thank J. Mecikalski for helpful comments.

Edited by: Y. Cheng

## References

- Ayers, G. P.: Air pollution and climate change: has air pollution suppressed rainfall over Australia?, *Clean Air and Environmental Quality*, 39, 51–57, 2005.
- Bendix, J., Thies, B., Cermak, J., and Nauß, T.: Ground Fog Detection from Space Based on MODIS Daytime Data – A Feasibility Study, *Weather Forecast.*, 20, 989–1005, 2005.
- Brunner, J. C., Ackerman, S. A., Bachmeier, A. S., and Rabin, R. M.: A Quantitative Analysis of the Enhanced-V Feature in Relation to Severe Weather, *Weather Forecast.*, 22, 853–872, 2007.
- Coakley, J. A., Bernstein, R. L., and Durkee, P. R.: Effects of ship-stack effluents on cloud reflectivity, *Science*, 237, 1020–1022, 1987.
- d’Entremont, R. P., and Larry, W.: Thomason: Interpreting Meteorological Satellite Images Using a Color-Composite Technique, *B. Am. Meteorol. Soc.*, 68, 762–768, 1987.
- Ferek, R. J., Garrett, T., Hobbs, P. V., Strader, S., Johnson, D., Taylor, J. P., Nielsen, K., Ackerman, A. S., Kogan, Y., Liu, Q., Albrecht, B. A., and Babb, D.: Drizzle Suppression in Ship Tracks, *J. Atmos. Sci.*, 57, 2707–2728, 2000.
- Goren, T., and Rosenfeld, D.: Decomposing aerosol cloud radiative effects into cover, liquid water path and Twomey components in Marine Stratocumulus, *Atmos. Res.*, 113, 378–393, doi:10.1016/j.atmosres.2013.12.008, 2013.
- Freud, E. and Rosenfeld, D.: Linear relation between convective cloud drop number concentration and depth for rain initiation, *J. Geophys. Res.*, 117, D02207, doi:10.1029/2011JD016457, 2012.
- Freud, E., Rosenfeld, D., and Kulkarni, J. R.: Resolving both entrainment-mixing and number of activated CCN in deep convective clouds, *Atmos. Chem. Phys.*, 11, 12887–12900, doi:10.5194/acp-11-12887-2011, 2011.
- Hillger, D. T., Kopp, T., Lee, D., Lindsey, C., Seaman, S., Miller, J., Solbrig, S., Kidder, S., Bachmeier, T., Jasmin, T., and Rink, T.: First-Light Imagery from Suomi NPP VIIRS, *B. Am. Meteorol. Soc.*, 94, 1019–1029, doi:10.1175/BAMS-D-12-00097.1, 2013.
- Inoue, T.: An instantaneous delineation of convective rainfall areas using split window data of NOAA-7 AVHRR, *J. Meteor. Soc. Japan*, 65, 469–481, 1987.
- Lensky, I. M. and Rosenfeld, D.: Estimation of precipitation area and rain intensity based on the microphysical properties retrieved from NOAA AVHRR data, *J. Appl. Meteorol.*, 36, 234–242, 1997.
- Lensky, I. M. and Rosenfeld, D.: Satellite-based insights into precipitation formation processes in continental and maritime convective clouds at nighttime, *J. Appl. Meteorol.*, 42, 1227–1233, 2003a.
- Lensky, I. M. and Rosenfeld, D.: A night rain delineation algorithm for infrared satellite data, *J. Appl. Meteorol.*, 42, 1218–1226, 2003b.
- Lensky, I. M. and Rosenfeld, D.: The time-space exchangeability of satellite retrieved relations between cloud top temperature and particle effective radius, *Atmos. Chem. Phys.*, 6, 2887–2894, doi:10.5194/acp-6-2887-2006, 2006.
- Lensky, I. M. and Rosenfeld, D.: Clouds-Aerosols-Precipitation Satellite Analysis Tool (CAPSAT), *Atmos. Chem. Phys.*, 8, 6739–6753, doi:10.5194/acp-8-6739-2008, 2008.
- Lindsey, D. T., Hillger, D. W., Grasso, L., Knaff, J. A., and Dostalek, J. F.: GOES Climatology and Analysis of Thunderstorms with Enhanced 3.9- $\mu\text{m}$  Reflectivity, *Mon. Weather Rev.*, 134, 2342–2353, 2006.
- Nakajima, T., and King, M. D.: Determination of the optical thickness and effective particle radius of clouds from reflected solar radiation measurements. Part I: Theory, *J. Atmos. Sci.*, 47, 1878–1893, doi:10.1175/1520-0469(1990)047<1878%3ADOTOTA>2.0.CO%3B2, 1990.
- Painemal, D., and Zuidema, P.: Assessment of MODIS cloud effective radius and optical thickness retrievals over the Southeast Pacific with VOCALS-REX in situ measurements, *J. Geophys. Res.*, 116, D24206, doi:10.1029/2011JD016155, 2011.
- Platnick, S., King, M. D., Ackerman, S. A., Menzel, W. P., Baum, B. A., Riédi, J. C., and Frey, R. A.: The MODIS cloud products: Algorithms and examples from Terra, *IEEE T. Geosci. Remote*, 41, 459–473, 2003.
- Radke, L. F., Coakley, J. A., and King, M. D.: Direct and remote sensing observations of the effects of ships on clouds, *Science*, 246, 1146–1149, 1989.
- Rosenfeld, D.: TRMM Observed First Direct Evidence of Smoke from Forest Fires Inhibiting Rainfall, *Geophys. Res. Lett.*, 26, 3105–3108, 1999.
- Rosenfeld, D.: Suppression of Rain and Snow by Urban and Industrial Air Pollution, *Science*, 287, 1793–1796, 2000.
- Rosenfeld, D. and Lensky, I. M.: Satellite-based insights into precipitation formation processes in continental and maritime convective clouds, *B. Am. Meteorol. Soc.*, 79, 2457–2476, 1998.
- Rosenfeld, D. and Woodley, W. L.: Closing the 50-year circle: From cloud seeding to space and back to climate change through precipitation physics. Chapter 6 of “Cloud Systems, Hurricanes, and the Tropical Rainfall Measuring Mission (TRMM)”, edited by: Tao, W.-K. and Adler, R., 234 pp., 59–80, *Meteorological Monographs* 51, AMS, 2003.
- Rosenfeld, D., Rudich, Y. and Lahav, R.: Desert dust suppressing precipitation- a possible desertification feedback loop, *P. Natl. Acad. Sci. USA*, 98, 5975–5980, 2001.
- Rosenfeld, D., Lahav, R., Khain, A. P., and Pinsky, M.: The role of sea-spray in cleansing air pollution over ocean via cloud processes, *Science*, 297, 1667–1670, 2002.
- Rosenfeld, D., Cattani, E., Melani, S., and Levizzani, V.: Considerations on daylight operation of 1.6-versus 3.7- $\mu\text{m}$  channel on NOAA and METOP satellites, *B. Am. Meteorol. Soc.*, 85, 873–881, 2004.
- Rosenfeld, D., Yu, X., and Dai, J.: Satellite retrieved microstructure of AgI seeding tracks in supercooled layer clouds, *J. Appl. Meteorol.*, 44, 760–767, 2005.
- Rosenfeld, D., Lensky, I. M., Peterson, J., and Gingis, A.: Potential impacts of air pollution aerosols on precipitation in Australia, *Clean Air and Environmental Quality*, 40, 2, 43–49, 2006.
- Rosenfeld, D., Fromm, M., Trentmann, J., Luderer, G., Andreae, M. O., and Servranckx, R.: The Chisholm firestorm:



- observed microstructure, precipitation and lightning activity of a pyro-cumulonimbus, *Atmos. Chem. Phys.*, 7, 645–659, doi:10.5194/acp-7-645-2007, 2007.
- Rosenfeld, D., Woodley, W. L., Lerner, A., Kelman, G., and Lindsey, D. T.: Satellite detection of severe convective storms by their retrieved vertical profiles of cloud particle effective radius and thermodynamic phase, *J. Geophys. Res.*, 113, D04208, doi:10.1029/2007JD008600, 2008.
- Rosenfeld, D., Yu, X., Liu, G., Xu, X., Zhu, Y., Yue, Z., Dai, J., Dong, Z., Dong, Y., and Peng, Y.: Glaciation temperatures of convective clouds ingesting desert dust, air pollution and smoke from forest fires, *Geophys. Res. Lett.*, 38, L21804, doi:10.1029/2011GL049423, 2011.
- Rosenfeld, D., Woodley, W. L., Khain, A., Cotton, W.R., Carrió, G., Ginis, I., and Golden, J. H.: Aerosol effects on Microstructure and Intensity of Tropical Cyclones, *B. Am. Meteorol. Soc.*, 93, 987–1001, 2012a.
- Rosenfeld, D., Williams, E., Andreae, M. O., Freud, E., Pöschl, U., and Rennó, N. O.: The scientific basis for a satellite mission to retrieve CCN concentrations and their impacts on convective clouds, *Atmos. Meas. Tech.*, 5, 2039–2055, doi:10.5194/amt-5-2039-2012, 2012b.
- Rudich, Y., Rosenfeld, D., and Khersonsky, O.: Treating clouds with a grain of salt, *Geophys. Res. Lett.*, 29, 2060, doi:10.1029/2002GL016055, 2002.
- Schickel, K. P., Hoffmann, H. E., and Kriebel, K. T.: Identification of icing water clouds by NOAA AVHRR satellite data, *Atmos. Res.*, 34, 177–183, 1994.
- Sullivan, J., Walton, C., Brown, J., and Evans, R.: Nonlinearity corrections for the thermal infrared channels of the Advanced Very High Resolution Radiometer: Assessment and recommendations, NOAA Tech. Rep. NESDIS 69, 31 pp., 1993.
- Thompson, G., Bullock, R., and Lee, T. F.: Using Satellite Data to Reduce Spatial Extent of Diagnosed Icing, *Weather Forecast.*, 12, 185–190, 1997.
- Woodley, W. L., Rosenfeld, D., and Strautins, A.: Identification of a seeding signature in Texas using multi-spectral satellite imagery, *J. Wea. Mod.*, 32, 37–52, 2000.